Journal of the Serbian Chemical Society
JSCS-info@shd.org.rs • www.shd.org.rs/JSCS

ACCEPTED MANUSCRIPT

Journal of the Serbian Chemical Society
JSCS-info@shd.org.rs • www.shd.org.rs/JSCS
J. Serb. Chem. Soc. **00(0)** 1-14 (2026)
JSCS–13610
Original scientific paper
Published DD MM, 2026

Hydrothermal synthesis of VO_2(B) and its phase transformation to VO_2(M): investigating metal-insulator transition behavior

AISHWARYA RAJGONDA PATIL,[1] KRISHNA CHAITANYA SOLASA,[1] SOURAV KUMAR,[2] SHREEYA RANE,[3] AND PALASH ROY CHOUDHURY[4]*

[1]*École Centrale School of Engineering, Mahindra University, Hyderabad, India,* [2]*Department of Metallurgical Engineering and materials science, IIT Indore, India,* [3]*Department of Physics, University of Warwick, UK, and* [4]*Mahindra University, Survey No: 62/1A, Bahadurpally, Jeedimetla, Hyderabad, Telangana 500043, India.*

(Received 1 November 2025; revised 16 December 2025; accepted 22 April 2026)

Abstract: In this study, VO_2(B) nanostructures were synthesized via a stabilizer-free hydrothermal route and successfully converted to VO_2(M) at 350 °C in just 30 minutes. This process offers a reduced thermal budget compared to established protocols, which generally require temperatures above 400 °C and durations exceeding one hour. The resulting urchin-like VO_2 nanostructures were characterized using a variety of techniques such as XRD, Raman Spectroscopy, SEM and DSC to investigate their structural evolution, surface morphology, and metal-insulator transition characteristics. The experimental results reveal that VO_2(B) predominantly transforms to VO_2(M) upon annealing at 350 ºC, with minor secondary oxide phases. Furthermore, the annealing at 450 ºC led to the complete phase transformation of VO_2 to V_2O_5, indicating the sensitivity of VO_2 to annealing temperature. This shows the insulator-to-metal transition temperature to be ~65 ºC, which is lower than the bulk VO_2 (~68 ºC), indicating modified transition behavior in the nanostructured samples. These results demonstrate that hydrothermally synthesized VO_2(B) can be converted to predominantly VO_2(M) by annealing at 350 °C for 30 min, enabling observation of a reversible metal–insulator transition near 65 °C.

Keywords: VO_2 nanostructures; hydrothermal synthesis; annealing effect; metal–insulator transition.

INTRODUCTION

Materials exhibiting Metal-Insulator-Transition (MIT) are used in Resistive Random-Access Memory (ReRAM) for non-volatile storage of data. Often this transition accompanies a corresponding change in their crystal structure and symmetry.[1] A transition between crystalline and amorphous phases may be

* Corresponding author. E-mail: palashroychoudhury@gmail.com
https://doi.org/10.2298/JSC251101022P

exploited for use in next-generation non-volatile memory because this transition corresponds to different resistive states.[2] Such materials can mimic neural synapses, which is essential in neuromorphic computing where devices emulate the human brain.[3] A gradual, analog variation in resistance near the MIT provides a means to model synaptic plasticity, achievable with materials that show progressive, voltage-dependent resistance changes.[4] Materials with MIT also hold promise in electronics beyond memory applications. They have the ability to replace conventional transistors in field-effect transistors (FETs), potentially enhancing energy efficiency and making way for ultra-low-power computing.[5] The sharp MIT in materials like VO_2 at specific temperatures can be used in thermal switches for managing heat flow in electronics.[6] These materials can act as thermal insulators below the transition temperature and as thermal conductors above it. Sharp MIT, which is associated with changes in crystal structure, may also exhibit changes in optical properties.[7] This property may be exploited to construct optical sensors and smart windows that can automatically modulate light of a certain frequency. Oxides undergoing MIT without concurrent magnetic transitions are promising candidates for spin-based quantum applications, where control over electronic phases without perturbing spin order is advantageous.[8] Some materials exhibit a high Seebeck coefficient near the MIT temperature that can be useful for thermoelectric applications.[9] This could enable the development of efficient thermoelectric generators for waste heat recovery, enhancing energy efficiency across various industries.

Materials undergoing a metal–insulator transition (MIT) have attracted significant interest due to the abrupt, reversible modulation of their properties. Among these, vanadium dioxide (VO_2) is a premier candidate for next-generation smart windows, thermal switches, and energy-responsive devices. Interest in VO_2 is particularly due to its fully reversible structural and electronic transition occurring at a near-ambient temperature of approximately 68 °C.

Vanadium dioxide possesses many possible crystalline forms or polymorphs, some of which are stable, and some are metastable. These include VO_2(M), VO_2(R), VO_2(A), VO_2(B), VO_2(C), VO_2(D) and VO_2 (Paramontroseite).[10] Out of these, the metal-insulator transition is associated between metallic VO_2(R) phase above 68 ºC and insulating VO_2(M) phase below 68 ºC. Many techniques have been used for VO_2 synthesis, including sol-gel,[11] magnetron sputtering,[12] chemical vapour deposition,[13] and hydrothermal method.[10,14] Among these, hydrothermal method is known to have minimal environmental impact and is often employed to synthesize metastable VO_2(B) phase. Vanadium pentoxide (V_2O_5) and ammonium metavanadate (NH_4VO_3) are commonly used vanadium sources in hydrothermal synthesis of VO_2. Commonly used reducing agents include oxalic acid,[15] hydrazine hydrate,[16] ethylene glycol,[17] octadecyl amine,[18] citric acid,[16] formic acid,[19] and formaldehyde.[20] Out of these, oxalic acid has been the most preferred reductant in

hydrothermal synthesis of VO_2 due to its low toxicity and ease of use. Zhu *et al.*[15] reported the synthesis of several types of VO_2(B) nanostructures by hydrothermal reaction combining ammonium metavanadate (NH_4VO_3) and oxalic acid at different time and temperatures. The resulting products had combinations of nanorods, nanoflakes and nanoflowers with the concentration of oxalic acid influencing their proportions.[15]

In this paper, we report a simple method of preparation of VO_2(M) via heat treatment of hydrothermally derived VO_2(B). The effect of different annealing conditions on the final products are characterized using X-ray diffraction (XRD), Raman Spectroscopy, scanning electron microscopy (SEM), UV–Vis spectroscopy and thermochemical properties have been studied using differential scanning calorimetry (DSC).

EXPERIMENTAL

Synthesis of VO_2 (B)

We synthesized VO_2(B) by hydrothermal reaction between commercial vanadium pentoxide powder (V_2O_5) and oxalic acid ($H_2C_2O_4{\cdot}H_2O$). Firstly, 0.73 g of V_2O_5 (1 mmol) was added into a beaker containing 40 mL de-ionized water. This mixture was stirred under ambient condition for 5 minutes using a magnetic stirrer. Then, 1.51 g of $H_2C_2O_4{\cdot}H_2O$ (3 mmol) was added to it and further stirred for 5 minutes, yielding a green solution indicating partial reduction. This solution was further continuously stirred at 80 ºC until aqueous solution turned into a clear transparent dark blue colour. The change in colour implied a reduction of vanadium from V^{5+} to V^{4+}. Then, this solution was transferred into a teflon lined stainless steel autoclave which was kept in a preheated oven (at 220 ºC) for 3 h to complete hydrothermal reaction for a duration of 3 h. The resulting bluish-black coloured precipitate was separated by centrifugation. This precipitate was then washed with ethanol and DI water several times to remove any contamination and was dried for 12 h at 60 ºC in an oven. This yielded black coloured vanadium dioxide powder (henceforth referred to as S-22). The resulting powder was subsequently ground in mortar and pestle and subjected to annealing in a tube-furnace at various temperatures. Figure 1 illustrates the various steps involved in the synthesis of vanadium oxide nanobelts.

Synthesis of VO_2(M)

VO_2(M) was derived from VO_2(B) through a controlled annealing process. A 500 mg sample from the as-synthesized VO_2 (S-22) was taken and annealed at different temperatures viz. 300º, 350º, 400º, and 450º (will henceforth be addressed as S-30, S-35, S-40, and S-45 respectively) for 30 minutes in quartz tubular vacuum furnace under low vacuum (10^{-2} mbar). Both the heating as well as cooling rates were maintained at 5 ºC/min.

Characterization

The crystal structure of the powder samples was characterized by XRD (Rigaku -D/MAX-RB) with Cu-Kα radiation (λ=0.154 nm). The data was analyzed using 'SMARTLab' software. The samples were scanned at 2θ range between 15º to 60º. Additionally, chemical and phase analysis were performed using Raman spectrometer (HORIBA, LabRAM) with a 633 nm laser excitation source. The microstructure and surface morphology of the sample were examined using Field Emission SEM (FE-SEM, JEOL). Differential scanning calorimetry (DSC, TA

Instruments, Model 2910) studies were performed to investigate phase transition behavior over a temperature range of 15-100 ºC using heating and cooling rates of 10 ºC/min. Optical transmittance measurements were carried out using a UV-Vis spectrometer (Ocean Insights) in the wavelength range of 200–800 nm to evaluate the optical of the material.

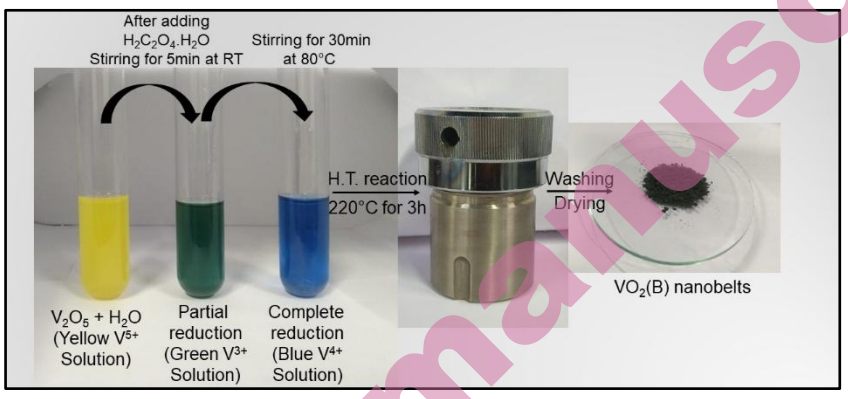

Figure 1. Schematic illustration of the entire reaction mechanism during hydrothermal synthesis of VO_2 nanobelts.

RESULTS AND DISCUSSION

Structural studies

The crystalline phase and purity of precursor, as-prepared and annealed samples were determined by XRD and obtained results are shown in Fig. 2. The bottom most spectrum is of the precursor V_2O_5 used for synthesis. The XRD patterns are readily assigned to V_2O_5 (ICDD: 09-0387), which reveals the purity of the precursor. S-22 shows the peaks in close agreement with VO_2(B) phase with miller indices (*hkl* planes) indicating growth of monoclinic VO_2(B) phase (ICDD: 01-84-7141). The lattice parameter values calculated are as follows: a = 12.04 Å, b = 3.68 Å, and c = 6.43 Å and it shows C2/m space group symmetry, with the strongest peaks at 2θ = 25.28, 29.09, 30.13, 37.01, 49.28, and 55.24º corresponding to (110), (002), (111), (202), (11$\bar{3}$) and (221) planes respectively. Additionally, VO_2(B) also exhibits a high degree of crystallinity, evidenced by the well-defined and strong XRD spectra. The diffraction peak at 2θ = 42.2º is indexed to the VO_2(M) phase (ICDD: 01-076-0456) for the (21$\bar{2}$) plane. There is no evidence of diffraction peaks corresponding to secondary oxide phases, such as V_2O_5. These results confirm that VO_2(B) phase is predominant, with no secondary oxides detected within XRD resolution limits. S-30 remains predominantly VO2(B), with trace reflections indicating the onset of a phase transition to VO_2(M).

From the analysis of XRD data, we observe that annealing at 350 °C sample S-35 resulted in the formation of predominantly monoclinic VO_2(M) phase, with minor secondary phases of V_2O_5 and V_3O_7. The lattice constants are a = 5.75 Å, b = 4.54 Å, and c = 5.38 Å, indicating a monoclinic structure with P21/c space group

symmetry. The peaks detected at 2θ = 27.79°, 37.01°, 39.72°, 42.20°, 51.24°, 55.45°, and 57.33° are assigned to the (001), (21$\bar{1}$), (020), (21$\bar{2}$), (22$\bar{1}$) (220), and (022) planes, respectively, for the monoclinic VO_2(M) phase (ICDD: 01-076-0456). The

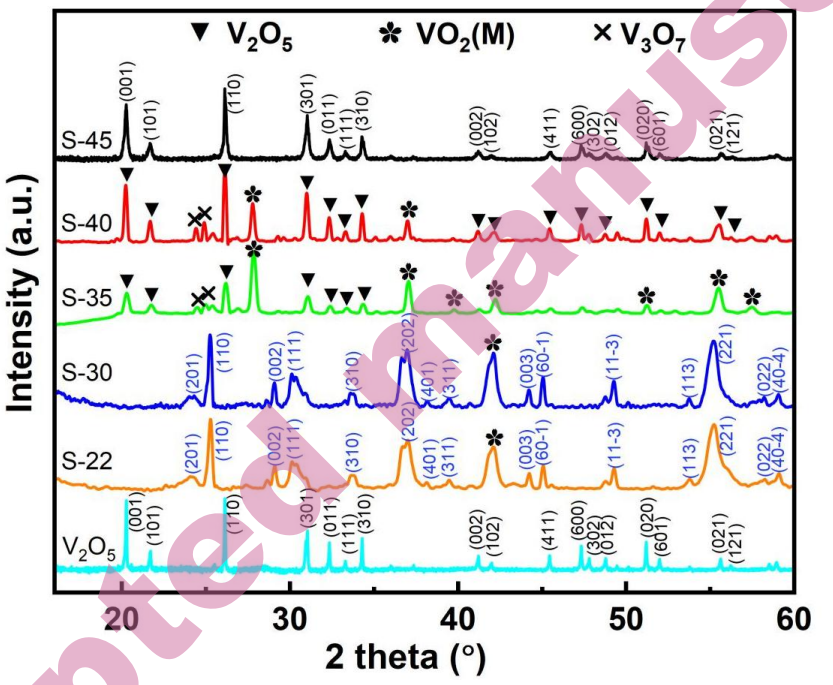

Figure 2. XRD patterns of pristine V_2O_5, the hydrothermally synthesized sample (S-22), and samples annealed at various temperatures (S-30, S-35, S-40, and S-45) for 30 minutes.

The XRD patterns of sample S-40 are a combination of phases with the presence of both VO_2 (M) and other peaks that belong to V_2O_5 and V_3O_7 (ICDD: 042-0876). It can be noted that with the increase in the annealing temperature, the intensities of the peaks of VO_2(M) decrease while the intensities of the V_2O_5 peaks increase, showing that reduced thermal stability of the VO_2 phase at elevated temperatures. In contrast, XRD spectra of S-45 show the presence of a complete oxidation of VO_2 to V_2O_5, which agrees well with existing literature.[21,22] This indicates that during high-temperature treatment, metastable VO_2 may have oxidized to change into its most thermodynamically stable phase, V_2O_5 (ICDD: 09-0387), which is the same as the precursor used for VO_2 synthesis. The average crystallite sizes estimated using Scherrer's formula for samples S-22, S-30, S-35, S-40, and S-45 are 19, 22, 24, 31 and 31 nm respectively.

Raman spectroscopy was used to analyze the structural and phase information in addition to the XRD. Raman spectra of S-22, the precursor V_2O_5, and the

annealed samples are shown in Figure 3(a) and (b). Characteristic peaks at 146 and 197 cm^{-1} are consistent with orthorhombic V_2O_5, indicating high purity and crystallinity of the precursor. The Raman modes at 285 and 406 cm^{-1} correspond to the bending modes of V=O bonds, and the one at 482 cm^{-1} is attributed to the bending of V–O–V. The peaks at 528 and 701 cm^{-1} are attributed to V–O bonds (combined stretching and bending vibrations). The 995 cm^{-1} peak arises from stretching of the V=O bond.[23-25]

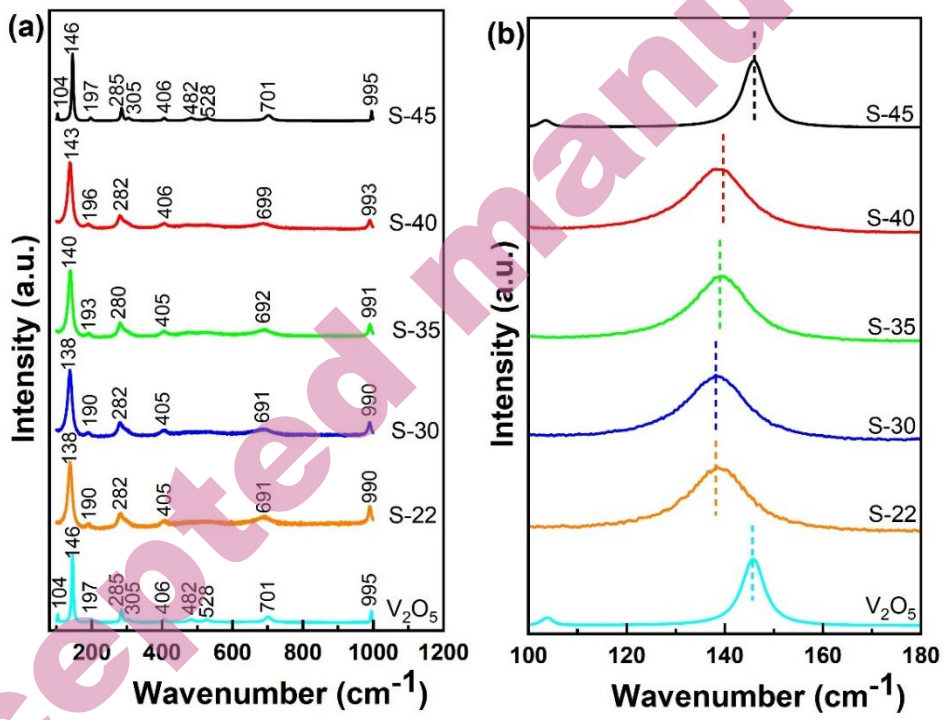

Figure 3. Raman spectra of all samples: (a) full spectra and (b) Raman spectra in the range of 135–150 cm^{-1} highlighting peak shift.

Furthermore, the Raman spectrum of the hydrothermally synthesized VO_2(B) phase (S-22) exhibits broad peaks at 138, 190, 282, 405, 691, and 990 cm^{-1}. The peaks at 138 and 282 cm^{-1} are attributed to V–O–V bending vibrations, while the 405 cm^{-1} peak corresponds to V–O–V stretching. The band at 691 cm^{-1} is associated with the coordination of three oxygen atoms around a vanadium center, and the strong peak at 990 cm^{-1} arises from V=O stretching vibrations. According to B. Cheng *et al*.[26] and S. Zhang *et al.,*[27] the above Raman peaks can be indexed to vibrational bands of VO_2(B) phase.

The sample S-30 exhibits characteristics similar to VO_2(B), indicating stability of phase up to this temperature. For the samples S-35 and S-40, we

observe a shift in peaks to higher frequencies (140, 280 and 692 cm^{-1}), indicating the formation of mixed phases and partial oxidation of VO_2(M). Finally, for the sample S-45, the Raman spectrum exhibits sharp peaks identical to those of the original V_2O_5 precursor, indicating complete oxidation. The zoomed region between 135-150 cm^{-1} (figure 3b) provides insights into peak shifts and phase transition from VO_2(B) to VO_2(M). Thus, the development of the Raman bands correspond well with the structural changes established using XRD and demonstrates the sensitivity of Raman spectroscopy to characterize the long-range order and local structural changes.

A detailed analysis of the Raman spectra for samples S-35 and S-40, which consist of mixed phases of VO_2(M) and V_2O_5, indicates that these phases cannot be distinctly resolved via Raman spectroscopy due to the overlap in their characteristic vibrational modes. Thus, phase identification in this case needs to be done from X-ray diffraction (XRD) data. Additionally, the Raman spectrum of sample S-45 exhibits features consistent with V_2O_5, indicating a phase transformation from VO_2 to V_2O_5, and closely matches the spectral signature of the V_2O_5 precursor. Raman spectroscopy thus serves as a complementary technique to XRD, confirming that our simple synthesis method reliably produces VO_2 with MIT behavior.

Morphological studies

The morphology of VO_2 nanostructures was analyzed with SEM. Figure 4 shows the SEM images of the as grown and annealed vanadium oxide nanostructures. For the samples S-22, shown in figure 4(a), multiple nanobelts are connected at the bottom and spread radially towards the top to form an urchin-like unit. The width of the nanobelts in the as-grown samples varies from ~50 to ~150 nm and length is in the sub-micrometer range. These urchin-like structures are symmetric with diameters ranging between 5–15 μm. This initial morphology is altered in the annealed samples. From the SEM image of S-30, we observe sharper needle-like structures compared to S-22, indicating denser, well-connected features with morphology that is consistent with the phase evolution observed from XRD data. The micrographs from the samples S-35 and S-40 show a somewhat mixed microstructure. The micrograph from the sample S-45 shows a significant change where needle-like features disappear, and the surface appears to develop granular features. Here we did not detect the existence of VO_2(M) phase and instead observe formation of pure V_2O_5. In summary, SEM analysis demonstrates that annealing temperatures strongly influence the morphological evolution of the nanostructures, while the associated changes in crystallinity and phase composition are confirmed by XRD data.

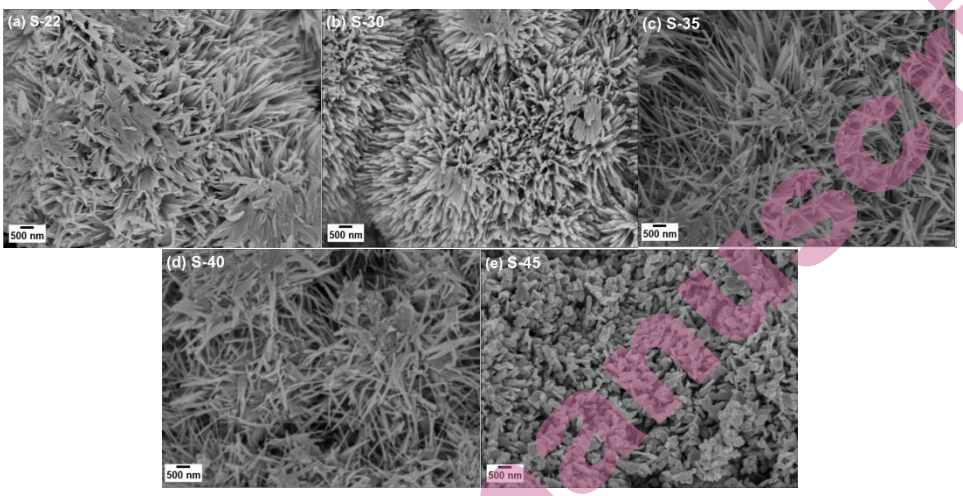

Figure 4. SEM images illustrating the morphology of nanostructure samples, (a) S-22, (b) S-30, (c) S-35, (d) S-40, and (e) S-45.

Optical properties

We performed Ultraviolet-Visible spectroscopy to study transmittance characteristics of vanadium oxide nanostructures. We calculated the band gap (optical) of these nanostructures with the help of the Tauc plot, which follows the equation:

$$(\alpha h\nu) = A(h\nu - E_g)^{\mathrm{n}} \quad (1)$$

where E_g is the band gap, α is absorption coefficient, $h\nu$ represents energy of light, A is constant, and n denotes nature of the transition.

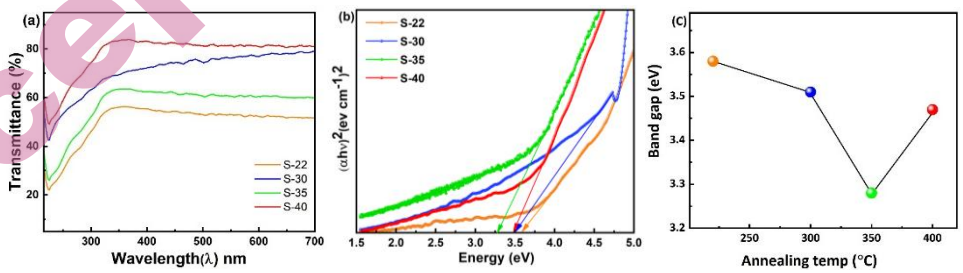

Figure 5. (a) Optical transmittance spectra of the samples annealed at various temperatures; (b) corresponding Tauc plots representing the magnitude of direct optical band gap; and (c) changes in optical band gap values with annealing temperature.

Figure 5 illustrates the effect of various annealing temperatures on the optical characteristics of the samples. The UV-Vis transmission spectra (Figure 5a) indicate that the transmittance generally increases with annealing temperature, indicating improved crystallinity in the samples.

We calculated the direct band gap energies, from the Tauc plots in figure 5(b), by extrapolating $(\alpha hv)^2$ versus energy (hv). The plots reveal a distinct trend of reduction in optical band gap values with increasing annealing temperature up to 350 ºC. Following this, there was a modest increase of the band gap at 400 ºC. Corresponding band gap values calculated from the Tauc plots. As shown in Figure 5(c), E_g decreases from 3.6 eV for the sample S-22 to a minimum of 3.3 eV for the sample S-35 and subsequently increases to 3.5 eV for sample S-40. Despite the minor morphological variations, the changes in E_g are primarily governed by phase transitions, as observed through XRD analysis. The increased band gap in hydrothermally synthesized urchin-like VO_2 samples with respect to bulk VO_2[28,29] (characteristically ~0.6–0.7 eV for the monoclinic structure) can be explained by several factors. Nanoscale crystallite size leads to quantum confinement effects, producing a wider band gap. Since VO_2(B) was found to have a wider than VO_2(M), the existence of both monoclinic (M) and metastable B phases together also contributes to wider band gap.[30] The lattice distortion and structural distortions also change the electrical structure. Defects and oxygen vacancies create localized states that change the band gap.[32] All these together are the potential reasons behind the much broader band gap in the VO_2 nanostructures.

Thermochromic properties

Figure 6 presents the differential scanning calorimetry (DSC) thermograms of VO_2(B) powders annealed at various temperatures (300–450 °C) for 30 minutes, with corresponding thermal parameters summarized in Table 1. The transition temperature (T_C) was determined as the midpoint between the endothermic peak temperature during heating and the exothermic peak temperature during cooling. Samples S-22, S-30, and S-45 do not display any prominent endothermic or exothermic peaks in the DSC curves. The absence of a clear metal–insulator transition in S-22 and S-30 can be attributed to the dominance of the VO_2(B) phase, which does not exhibit a sharp transition like monoclinic VO_2(M). In addition, broader XRD peaks were observed for these samples, indicating reduced crystallinity. This leads to weaker cooperative lattice distortion, which is necessary for an abrupt structural transition. For sample S-45, the disappearance of the transition is due to the dominant V_2O_5 phase as identified by XRD, which does not exhibit a metal–insulator transition in this temperature range.[31,32]

For the samples S-35 and S-40, endothermic peak maximum during the heating cycle remains nearly constant at ~ 73 ºC. However, the exothermic peak during the cooling cycle shifts slightly from 57 ºC for S-35 to 59 ºC for S-40. As a result, the calculated transition temperature (T_C) (determined as the midpoint between heating and cooling peaks) increases only slightly from 65 ºC (for S-35) to 66 ºC (for S-40). Simultaneously, the thermal hysteresis width (ΔT), calculated as the difference between the heating and cooling transition temperatures, decreases from 16 ºC to 14 ºC. A reduction in magnitude of ΔT suggests an

improved reversibility of the structural transformation. This behavior correlates with the enhanced crystallinity observed in the XRD patterns of S-40 relative to S-35, implying that improved structural ordering contributes to a more uniform and coherent phase transition. The observed T_C values are slightly lower than the values of bulk VO_2(M), which is typically ~68 ºC. This reduction to ~65 ºC can be attributed to residual VO_2(B) and nanocrystalline interfaces. Overall, the appearance and sharpness of the metal–insulator transition are strongly governed by phase composition and crystallinity. Samples dominated by VO_2(B) or V_2O_5 do not exhibit a prominent transition, whereas samples containing predominantly monoclinic VO_2(M) phase exhibit a distinct and reversible MIT. The improved crystallinity observed in XRD for S-35 and S-40 contributes to a narrower hysteresis width and more consistent structural transformation. Similar reductions in transition temperature and broadening of the MIT in nanocrystalline or mixed-phase VO_2 systems have been reported in previous studies, where strain effects and phase heterogeneity were found to influence MIT behavior.[33-35]

The reduction in hysteresis width may be attributed to partial conversion of VO_2(B) to V_2O_5, as detected by X-ray diffraction (XRD). It may also be due to the presence of defects at the interface.[34] In contrast, samples S-35 and S-40 clearly exhibit a phase transition, consistent with phase evolution confirmed by XRD.

In addition, the sample S-35 exhibited an average transmittance up to about 59% obtained at room temperature (300K), which is comparable or slightly improved compared to published literature.[32,33] Phase transformation in VO_2 was clearly observed for samples annealed at 350 ºC, demonstrating that this procedure is simple and energy efficient. For observable phase transition in VO_2 prepared by reduction of V_2O_5, the required annealing temperature is often above 400 ºC and time more than 1 h as reported in previous works.[36,37] Our method lowers the thermal budget by achieving VO_2 phase transformation faster (30 minutes) and at a lower annealing temperature than previously reported schemes. The resulting VO_2(M) nanostructures exhibit reversible thermochromic behavior.

Integrating XRD, Raman, optical, and DSC analyses indicates a distinct phase–property correlation across the synthesized, annealed nanostructures. Specimens dominated by VO_2(B) (S-22, S-30) are characterized by broadened diffraction profiles and wider band gaps and also lacking an observable MIT. In contrast, the formation of predominantly VO_2(M) phase at 350 °C (S-35) is associated with significant band gap narrowing and the emergence of a well-defined, reversible MIT near 65 °C. Progressive oxidation from 400–450 °C results in formation of V2O5, which effectively suppresses this transition. These findings show that phase purity and crystallinity are major factors for thermochromic properties and MIT in these nanostructures.

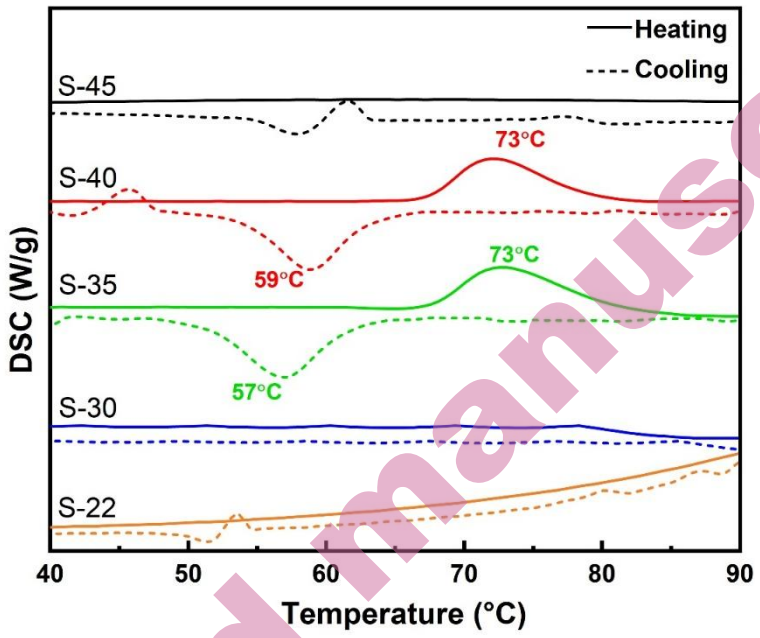

Figure 6. DSC results illustrating a well-defined, reversible metal–insulator transition exclusively in the specimens annealed at 350 °C and 400 °C. In contrast, other samples exhibit a featureless thermal profile indicating the absence of a detectable phase transition..

Table 1. Comparison of phase transition temperatures obtained from DSC analysis during heating and cooling cycles.

Sample	Annealing temp. (°C)	Dominant phase	Secondary phase	T_{Heat} (°C)	T_{Cool} (°C)	T_C (°C)	ΔT (°C)
S-22	as-synthesized	VO_2(B)	-	-	-	-	-
S-30	300	VO_2(B)	VO_2(M)	-	-	-	-
S-35	350	VO_2(M)	V_2O_5, V_3O_7	73	57	65	16
S-40	400	V_2O_5	VO_2(M), V_3O_7	73	59	66	14
S-45	450	V_2O_5	-	-	-	-	-

CONCLUSION

VO_2 nanostructures were synthesized using a stabilizer-free hydrothermal process followed by controlled thermal annealing. The as-prepared sample (S-22) predominantly exhibited the metastable VO_2(B) phase with high crystallinity. Annealing at 350 °C resulted in predominantly monoclinic VO_2(M), accompanied by minor secondary phases of V2O5 and V_3O_7. With further increase in annealing temperature to 400 °C, V_2O_5 becomes the predominant phase while the relative intensity of VO_2(M) decreases, indicating progressive oxidation of VO_2. Annealing at 450 °C resulted in the complete oxidation to V_2O_5. While the

crystallite size increases with annealing temperature, the band gaps exhibit a non-monotonic variation with annealing temperature or phase variation. The sample annealed at 350 ºC shows room temperature average transmission at 59% and phase transition temperature of ~65 ºC. Samples S-35 and S-40 exhibit clear, reversible phase transformation between temperatures of 65-66 ºC. In summary, we demonstrate the tunability of phase composition and transition behavior in annealed VO_2 nanostructures and provide insight into the relationship between structural evolution and metal–insulator transition behavior. Our demonstration of a cost-effective and stabilizer-free hydrothermal synthesis also offers a reduced thermal budget route for scalable vanadium dioxide production, enabling controlled phase evolution and metal–insulator transition behavior in VO_2 nanostructures.

И З В О Д

ХИДРОТЕРМАЛНА СИНТЕЗА И ФАЗНА ТРАНСФОРМАЦИЈА VO_2(B) У VO_2(M): ИСТРАЖИВАЊЕ ПРЕЛАЗА МЕТАЛ-ИЗОЛАТОР

AISHWARYA RAJGONDA PATIL,[1] KRISHNA CHAITANYA SOLASA,[1] SOURAV KUMAR,[2] SHREEYA RANE,[3] AND PALASH ROY CHOUDHURY[4]

[1]École Centrale School of Engineering, Mahindra University, Hyderabad, India, [2]Department of Metallurgical Engineering and materials science, IIT Indore, India, [3]Department of Physics, University of Warwick, UK, and [4]Mahindra University, Survey No: 62/1A, Bahadurpally, Jeedimetla, Hyderabad, Telangana 500043, India.

У овом раду, VO_2(B) наноструктуре су синтетизоване хидротермалним путем без стабилизатора и успешно конвертоване у VO_2(M) на 350 °C за само 30 минута. Овим поступком се постиже уштеда енергије у односу на уобичајене поступке, који генерално захтевају температуре више од 400 °C и трајање дуже од једног сата. Добијене VO_2 наноструктуре са игличастим честицама су окарактерисане коришћењем различитих техника као што су XRD, раманска спектроскопија, SEM и DSC како би се испитао фазни састав, морфологија и карактеристике прелаза метал-изолатор. Експериментални резултати показују да се VO_2(B) претежно трансформише у VO_2(M) након калцинације на 350 ºC, са малим уделом секундарних оксидних фаза. Додатно, жарење на 450 ºC довело је до потпуне фазне трансформације VO_2 у V_2O_5, што указује на осетљивост VO_2 на температуру калцинације. Температура прелаза изолатор-метал је ~65 ºC, што је ниже него за VO_2 у комаду (~68 ºC), што указује на модификовано понашање прелаза у наноструктурним узорцима. Ови резултати показују да се хидротермално синтетисани VO_2(B) може трансформисати претежно у VO_2(M) жарењем на 350 °C током 30 минута, што омогућава реверзибилни прелаз метал-изолатор близу 65 °C.

(Примљено 1. новембра 2025; ревидирано 16. децембра 2025; прихваћено 22. априла 2026.)

REFERENCES

1. A. B. Georgescu, A. J. Millis, *Commun. Phys.* **5** (2022) 135 (https://doi.org/10.1038/s42005-022-00909-z)
2. A. Moatti, R. Sachan, J. Narayan, *J. Appl. Phys.* **128** (2020) 045302 (https://doi.org/10.1063/5.0006671)

3. G. Ekinci, B. Özkal, S. Kazan, *ACS Omega* **9** (2024) 26235–26244 (https://doi.org/10.1021/acsomega.4c02001)
4. A. R. Galloni, Y. Yuan, M. Zhu, H. Yu, R. S. Bisht, C.-T. M. Wu, C. Grienberger, S. Ramanathan, A. D. Milstein, *Proc. Natl. Acad. Sci.* **121** (2024) e2318362121 (https://doi.org/10.1073/pnas.2318362121)
5. N. Shukla, A. V Thathachary, A. Agrawal, H. Paik, A. Aziz, D. G. Schlom, S. K. Gupta, R. Engel-Herbert, S. Datta, *Nat. Commun.* **6** (2015) 7812 (https://doi.org/10.1038/ncomms8812)
6. S. Jessadaluk, N. Khemasiri, P. Rattanawarinchai, S. Rahong, A. Rangkasikorn, N. Kayunkid, S. Wirunchit, A. Klamchuen, J. Nukeaw, *Jpn. J. Appl. Phys.* **58** (2019) SDDE12 (https://doi.org/10.7567/1347-4065/ab0aca)
7. A. Ainabayev, B. Walls, D. Casey, D. Caffrey, D. Mullarkey, A. McGlinchey, A. Khare, A. Tikhonov, C. Ilhan, D. Brennan, S. J. McCormack, I. Shvets, *J. Phys. Chem. C* **127** (2023) 24432–24442 (https://doi.org/10.1021/acs.jpcc.3c06057)
8. R. Zhang, Q. S. Fu, C. Y. Yin, C. L. Li, X. H. Chen, G. Y. Qian, C. L. Lu, S. L. Yuan, X. J. Zhao, H. Z. Tao, *Sci. Rep.* **8** (2018) 17093 (https://doi.org/10.1038/s41598-018-35490-5)
9. Q. Song, J. Zhou, L. Meroueh, D. Broido, Z. Ren, G. Chen, *Appl. Phys. Lett.* **109** (2016) 263902 (https://doi.org/10.1063/1.4973292)
10. M. Li, S. Magdassi, Y. Gao, Y. Long, *Small* **13** (2017) 1701147 (https://doi.org/10.1002/smll.201701147)
11. M. M. Seyfouri, R. Binions, *Sol. Energy Mater. Sol. Cells* **159** (2017) 52–65 (https://doi.org/10.1016/j.solmat.2016.08.035)
12. F. Xu, X. Cao, Z. Shao, G. Sun, S. Long, T. Chang, H. Luo, P. Jin, *ACS Appl. Mater. Interfaces* **11** (2019) 4712–4718 (https://doi.org/10.1021/acsami.8b20794)
13. D. Malarde, M. J. Powell, R. Quesada-Cabrera, R. L. Wilson, C. J. Carmalt, G. Sankar, I. P. Parkin, R. G. Palgrave, *ACS Omega* **2** (2017) 1040–1046 (https://doi.org/10.1021/acsomega.7b00042)
14. C. Wang, H. Xu, C. Wang, T. Liu, S. Yang, Y. Nie, X. Guo, X. Ma, X. Jiang, *J. Alloys Compd.* **877** (2021) 159888 (https://doi.org/10.1016/j.jallcom.2021.159888)
15. J. Ni, W. Jiang, K. Yu, Y. Gao, Z. Zhu, *Electrochim. Acta* **56** (2011) 2122–2126 (https://doi.org/10.1016/j.electacta.2010.11.093)
16. S. R. Popuri, M. Miclau, A. Artemenko, C. Labrugere, A. Villesuzanne, M. Pollet, *Inorg. Chem.* **52** (2013) 4780–4785 (https://doi.org/10.1021/ic301201k)
17. S. Zhang, Y. Li, C. Wu, F. Zheng, Y. Xie, *J. Phys. Chem. C* **113** (2009) 15058–15067 (https://doi.org/10.1021/jp903312h)
18. B.-R. Jia, M.-L. Qin, Z.-L. Zhang, S.-M. Li, X.-L. Wang, M. Huang, H.-Y. Wu, Z. Chen, X. Lu, L. Zhang, X-H. Qu, *J. Alloys Compd.* **704** (2017) 79–88 (https://doi.org/10.1016/j.jallcom.2017.02.046)
19. J. Liu, Q. Li, T. Wang, D. Yu, Y. Li, *Angew. Chemie Int. Ed.* **43** (2004) 5048–5052 (https://doi.org/10.1002/anie.200460104)
20. K.-C. Zhou, D.-M. Cao, Z.-Y. Li, *Trans. Nonferrous Met. Soc. China* **16** (2006) 517–521 (https://doi.org/10.1016/S1003-6326(06)60090-3)
21. H. H. Afify, S. A. Hassan, M. Obaida, A. Abouelsayed, *Phys. E Low-dimensional Syst. Nanostruct.* **114** (2019) 113610 (https://doi.org/10.1016/j.physe.2019.113610)
22. D. Alie, L. Gedvilas, Z. Wang, R. Tenent, C. Engtrakul, Y. Yan, S. E. Shaheen, A. C. Dillon, C. Ban, *J. Solid State Chem.* **212** (2014) 237–241 (https://doi.org/10.1016/j.jssc.2013.10.023)

23. M. Dhananjaya, N. G. Prakash, A. L. Narayana, O. M. Hussain, *Appl. Phys. A Mater. Sci. Process.* **124** (2018) 185 (https://doi.org/10.1007/s00339-017-1522-0)
24. D. Dreifus, M. P. F. Godoy, A. C. Rabelo, A. D. Rodrigues, Y. G. Gobato, P. C. Camargo, E. C. Pereira, A. J. A. De Oliveira, *J. Phys. D. Appl. Phys.* **48** (2015) 445002 (https://doi.org/10.1088/0022-3727/48/44/445002)
25. D. Surya Bhaskaram, R. Cheruku, G. Govindaraj, *J. Mater. Sci. Mater. Electron.* **27** (2016) 10855–10863 (https://doi.org/10.1007/s10854-016-5194-x)
26. B. Cheng, H. Zhang, Q. Li, J. Liu, B. Liu, *Inorganics* **10** (2022) 122 (https://doi.org/10.3390/inorganics10080122)
27. S. Zhang, Z. Zou, T. Lv, S. Li, Y. Zhang, *Int. J. Electrochem. Sci.* **15** (2020) 7203–7213 (https://doi.org/10.20964/2020.08.05)
28. H. W. Verleur, A. S. Barker, C. N. Berglund, *Rev. Mod. Phys.* **40** (1968) 737 (https://doi.org/10.1103/RevModPhys.40.737)
29. K. Schneider, *J. Mater. Sci. Mater. Electron.* **31** (2020) 10478–10488 (https://doi.org/10.1007/s10854-020-03596-0)
30. Meenu, P. Kumar, B. S. Dehiya, *J. Nanosci. Technol.* **5** (2019) 584–586 (https://doi.org/10.30799/jnst.195.19050102)
31. F. Mehmood, R. Pachter, N. R. Murphy, W. E. Johnson, C. V. Ramana, *J. Appl. Phys.* **120** (2016) 191–195 (https://doi.org/10.1063/1.4972038)
32. F. Arteaga-Cardona, A. P. Franco-Bacca, F. Cervantes-Alvarez, J. J. Alvarado-Gil, N. R. Silva-González, U. Salazar-Kuri, *Appl. Phys. A* **127** (2021) 159 (https://doi.org/10.1007/s00339-021-04309-y)
33. C. Xu, G. Liu, M. Li, K. Li, Y. Luo, Y. Long, G. Li, *Mater. Des.* **187** (2020) 108396 (https://doi.org/10.1016/j.matdes.2019.108396)
34. K. L. Gurunatha, S. Sathasivam, J. Li, M. Portnoi, I. P. Parkin, I. Papakonstantinou, *Adv. Funct. Mater.* **30** (2020) 27–31 (https://doi.org/10.1002/adfm.202005311)
35. L. Liu, F. Cao, T. Yao, Y. Xu, M. Zhou, B. Qu, B. Pan, C. Wu, S. Wei, Y. Xie, *New J. Chem.* **36** (2012) 619–625 (https://doi.org/10.1039/C1NJ20798A)
36. B. S. Beckerle, A. B. Cezar, I. T. Neckel, W. H. Schreiner, A. G. Bezerra Jr., I. L. Graff, J. Varalda, D. H. Mosca, *J. Appl. Phys.* **134** (2023) 123-101 (https://doi.org/10.1063/5.0169279)
37. S. A. Corr, M. Grossman, Y. Shi, K. R. Heier, G. D. Stucky, R. Seshadri, *J. Mater. Chem.* **19** (2009) 4362–4367 (https://doi.org/10.1039/B900982E).